https://doi.org/10.5194/egusphere-2023-1834
Preprint. Discussion started: 16 August 2023

AI-derived 3D cloud tomography from geostationary 2D satellite data

Sarah Brüning[1], Stefan Niebler[2], and Holger Tost[1]

[1]Institute for Physics of the Atmosphere, Johannes Gutenberg University Mainz, Johann-Joachim-Becher-Weg 21, Mainz, 55128, Rhineland-Palatine, Germany
[2]Institute of Computer Science, Johannes Gutenberg University Mainz, Staudingerweg 9, Mainz, 55128, Rhineland-Palatine, Germany

Correspondence: Sarah Brüning (sbruenin@uni-mainz.de)

Abstract. Satellite instruments provide spatially extended data with a high temporal resolution on almost global scales. However, nowadays, it is still a challenge to extract fully three-dimensional data from the current generation of satellite instruments, which either provide horizontal patterns or vertical profiles along the orbit track. Following this, we train a neural network in this study to generate three-dimensional cloud structures from MSG SEVIRI satellite data in high spatio-temporal resolution. We evaluate the derived artificial intelligence-based predictions against the along-track radar reflectivity from the CloudSat satellite. By inferring the pixel-wise cloud column to the satellite's full disk, our results emphasize that spatio-temporal dynamics can be delineated for the whole domain. Robust reflectivities are derived for different cloud types with a clear distinction regarding the cloud's intensity, height, and shape. Cloud-free pixels tend to be over-represented because of the high imbalance between cloudy and clear-sky samples. The average error (RMSE) spans about 7.5 % (3.41 dBZ) of the total value range enabling the advanced analysis of vertical cloud properties. Although we receive high accordance between radar data and our predictions, the quality of the results varies with the complexity of the cloud structure. The representation of multi-level and mesoscale clouds is often simplified. Despite current limitations, the obtained results can help close current data gaps and exhibit the potential to be applied to various climate science questions, like the further investigation of deep convection through time and space.

1 Introduction

Clouds and their interdependent feedback mechanisms have been a source of uncertainty in Earth system models for decades. As they influence different spheres of the environment, their accurate representation is needed for an improved understanding of interconnected dynamics (Norris et al., 2016; Stevens and Bony, 2013; Vial et al., 2013). Although their connection to atmospheric gases and general circulation patterns is evident, further quantification is required (Rasp et al., 2018; Shepherd, 2014; Bony et al., 2015). The pressing need to adapt society to climate change emphasizes the need for reliable data today more than ever (Dubovik et al., 2021).

In recent years, observational data from remote sensing instruments have been proven reliable in investigating cloud properties on multiple scales (Jeppesen et al., 2019). Although these approaches drove research forward, techniques to detect

https://doi.org/10.5194/egusphere-2023-1834
Preprint. Discussion started: 16 August 2023

three-dimensional (3D) cloud structures still need to be developed (Bocquet et al., 2015). While passive sensors like geostationary satellites monitor the uppermost atmospheric layer from space with a two-dimensional (2D) output (Noh et al., 2022), active radar penetrates the cloud top and delivers detailed information on the subjacent distribution (Barker et al., 2011). The latter provides a thorough but spatially and temporally limited perspective (Wang et al., 2023). An approximation of cloud physical properties like the cloud optical thickness, the effective radius, or the cloud water path is obtainable using the satellite's specificity at different wavelengths (Thies and Bendix, 2011; Platnick et al., 2017). While this analysis often rests upon subjective labeling or fixed thresholds, it is under the risk of bias (Stubenrauch et al., 2013). Besides, passive sensors lack the inherent sensitivity to detect information from deep within cloud layers to accurately differentiate cloud types (Noh et al., 2022). At this point, combining data sources can substantially leverage the quality of analysis (Amato et al., 2020; Steiner et al., 1995). A joined use of different instruments to derive comprehensive 3D structures has been investigated before either by statistical algorithms (Miller et al., 2014; Seiz and Davies, 2006; Noh et al., 2022), the integration of radiative transfer approaches (Forster et al., 2021; Zhang et al., 2012), or the derivation of the multi-angle geometry of neighboring clouds (Barker et al., 2011; Ham et al., 2015). The large-scale generability of these methods is expandable since their 3D results are limited to the cloud's spatial vicinity (Leinonen et al., 2019). To this day, no interpolation of the cloud vertical column to a large-scale, supra-regional perspective exists (Wang et al., 2023; Dubovik et al., 2021).

Emerging facilitators of data availability, like open-data policies and improved technological standards, open up unforeseen possibilities (Jeppesen et al., 2019; Liu et al., 2016; Reichstein et al., 2019). These developments promote further integration of computer science methods in climate science as they enable effective processing of memory-consuming satellite data (Irrgang et al., 2021; Rasp et al., 2018). With an accompanying potential for substantial growth in knowledge (Amato et al., 2020; Watson-Parris, 2021), ever-growing quantities of data surpass the capability of the human mind to extract explainable information efficiently (Lee et al., 2021; Karpatne et al., 2019). Here, the usage of artificial intelligence (AI) has been assigned a primary role (Runge et al., 2019). Cloud properties have been analyzed before using Machine Learning (ML) algorithms (Reichstein et al., 2019; Marais et al., 2020), but recent technological advances enable unprecedented operations, especially on big data (Amato et al., 2020). Suitable to identify spatial, spectral, and temporal patterns, Deep-Learning (DL) based networks outperform classical ML approaches in terms of time efficiency and feasibility (Jeppesen et al., 2019; Hilburn et al., 2020; Le Goff et al., 2017). Their adaptation to applications in climate science offer new perspectives for the scientific community and the general public (Rasp et al., 2018; Rolnick et al., 2022; Jones, 2017).

So far, the possibility of investigating cloud properties by the usage of DL algorithms has been shown in various applications. These comprise detecting and segmenting cloud fields (Drönner et al., 2018; Jeppesen et al., 2019; Lee et al., 2021; Le Goff et al., 2017; Tarrio et al., 2020; Cintineo et al., 2020) or classifying distinct cloud types from meteorological satellites and aerial imagery (Marais et al., 2020; Wang et al., 2023). Regressive models were used to investigate the delineation of rain rates (Han et al., 2022) or convective onset (Pan et al., 2021) for an improved weather forecast. While the results indicate an improvement in resource efficiency, they are predominately restricted to horizontal processes of the cloud field. Reconstructing the cloud vertical column can deliver insights into 3D dynamics (van den Heuvel et al., 2020; Leinonen et al., 2019). Current studies by Hilburn et al. (2020) and Leinonen et al. (2019) use AI techniques such as convolutional neural networks (CNN)

https://doi.org/10.5194/egusphere-2023-1834
Preprint. Discussion started: 16 August 2023

and conditional generative adversarial networks (CGAN) to address this issue. In both cases, they provide pixel-based cloud reflectivities similar to the input of an active radar (Wang et al., 2023). Nevertheless, the large-scale spatial coherence cannot be fully resolved. Prior studies face limitations when predicting multi-layer and mesoscale events (Hilburn et al., 2020). Since clouds in the real world are highly complex, spatially restricted models fail to reconstruct comprehensive cloud structures (Hu et al., 2021). Image prediction approaches like the UNet (Ronneberger et al., 2015; Jiao et al., 2020; Wieland et al., 2019) display a promising start to reconstruct the ground truth data and to provide the indicators for predicting clouds in 3D with its adjacent boundaries, shadow locations, and geometries. Defining each cloud as a connected entity can lead to a more realistic representation of the actual distribution of clouds and their interactions around the globe (Jiao et al., 2020; Hu et al., 2021; Wang et al., 2023).

This study combines the benefits of active and passive instruments by a modified Res-UNet (Diakogiannis et al., 2020; Hu et al., 2021) to reconstruct the 3D vertical cloud column of volumetric radar data from 2D geostationary satellite data. In contrast to former studies focusing on the pixel-based perspective along the radar track, the spatial connectivity between individual pixels is preserved to predict the results for the spatial extent of the input image and infer them to a large-scale area on the satellite full disk (FD). The goal is to derive a spatio-temporal consistent cloud tomography based exclusively on real-world data. This information can be used to improve the availability and quality of 3D resolved cloud structures, especially in data-sparse regions, and their further investigation in a hydro-climatological context.

2 Methods

2.1 Data

Our approach uses observational data from two different remote sensing sensors to predict a 3D cloud tomography. The input data for the network originates a geostationary satellite (EUMETSAT Data Services, 2023). This sensor observes the Earth surface from space providing 2D image data in a high resolution. The ground truth of the study is derived from an active radar orbiting the globe on a sinusoidal track (CloudSat Data Processing Center, 2023). It receives information on the cloud reflectivity during this flight, point by point, which are combined into vertical profiles. Here, we feed the satellite data into the model to delineate the relationships needed to accurately reconstruct these profiles.

2.1.1 Satellite data

Data from the European Organisation for the Exploitation of Meteorological Satellites (EUMETSAT) Spinning Enhanced Visible and InfraRed Imager (SEVIRI) instrument on the Meteosat Second Generation (MSG) satellite displays the input for the network (Schmetz et al., 2002). Observing the Earth's surface in intervals of 15 min and 3 km at nadir, it provides information in 11 channels centered within wavelengths from 0.6–132 μm (Benas et al., 2017). While the first three channels are sensitive to reflected solar radiation, the others measure surface emissions within the near to thermal infrared spectrum. These channels can be applied to approximate cloud physical properties (Sieglaff et al., 2013). Regions close to the poles are

https://doi.org/10.5194/egusphere-2023-1834
Preprint. Discussion started: 16 August 2023

discarded due to reduced sensor accuracy at the satellite's outer boundaries (Bedka et al., 2010). The final area of interest (AOI) comprises an extent between 60° in all directions and represents the new FD. All satellite images are resampled to a geographic grid using the global reference system WGS84 (Drönner et al., 2018).

2.1.2 Radar data

Within the CloudSat (CS) GEOPROF-2B product, a nadir-looking 94 GHz active radar delivers information on the cloud reflectivity in logarithmic dBZ scale (Stephens et al., 2008). The radar scenes reflect the predominant cloud structure at the given transect with a horizontal resolution of 1.1 km and a vertical bin size of 240 m in 125 height levels (Guillaume et al., 2018). The total vertical extent comprises 0–30 km, from the mean ground surface to the lower stratosphere. Information on the reflectivity obtained by the radar displays the ground truth used to evaluate the model results.

2.1.3 Matching scheme

Matching the MSG SEVIRI scenes and the overflight of the CloudSat radar extracts the training data of the study. The framework automatically identifies the radar overpass over the satellite domain and its flight direction (Fig. 1). Figure 1 pictures a schematic view of the matching scheme. First, the timestamps and locations of both data sources are compared. Suppose the current flight coordinates lie within the satellite AOI. In that case, the direction of flight is determined by the coordinates of the first and last entry of the radar file. The most northward and southward locations define the radar's direction as ascending or descending. We place the first image at the lower-right or upper-left corner of the radar within the satellite FD. To derive continuous tracks, a moving-window approach is applied with a 50 % overlap between single images starting with the most northern (descending) or southern (ascending) location (Denby, 2020; Jeppesen et al., 2019). Each image contains the native satellite channels leading to an input size of 11 x 128 x 128 pixels [C x X x Y]. The radar track is centered within each image displaying the vertical column along the horizontal transect [Z x XY] (Fig. 1). A spatial join of the radar data coordinates fits the resolution between both sensors. For that purpose, the local maximum reflectivity of each pixel area returns the factor to coarse-grain the radar data. This filter results in a partial information loss at the edges of individual clouds (Jordahl et al., 2020).

https://doi.org/10.5194/egusphere-2023-1834
Preprint. Discussion started: 16 August 2023

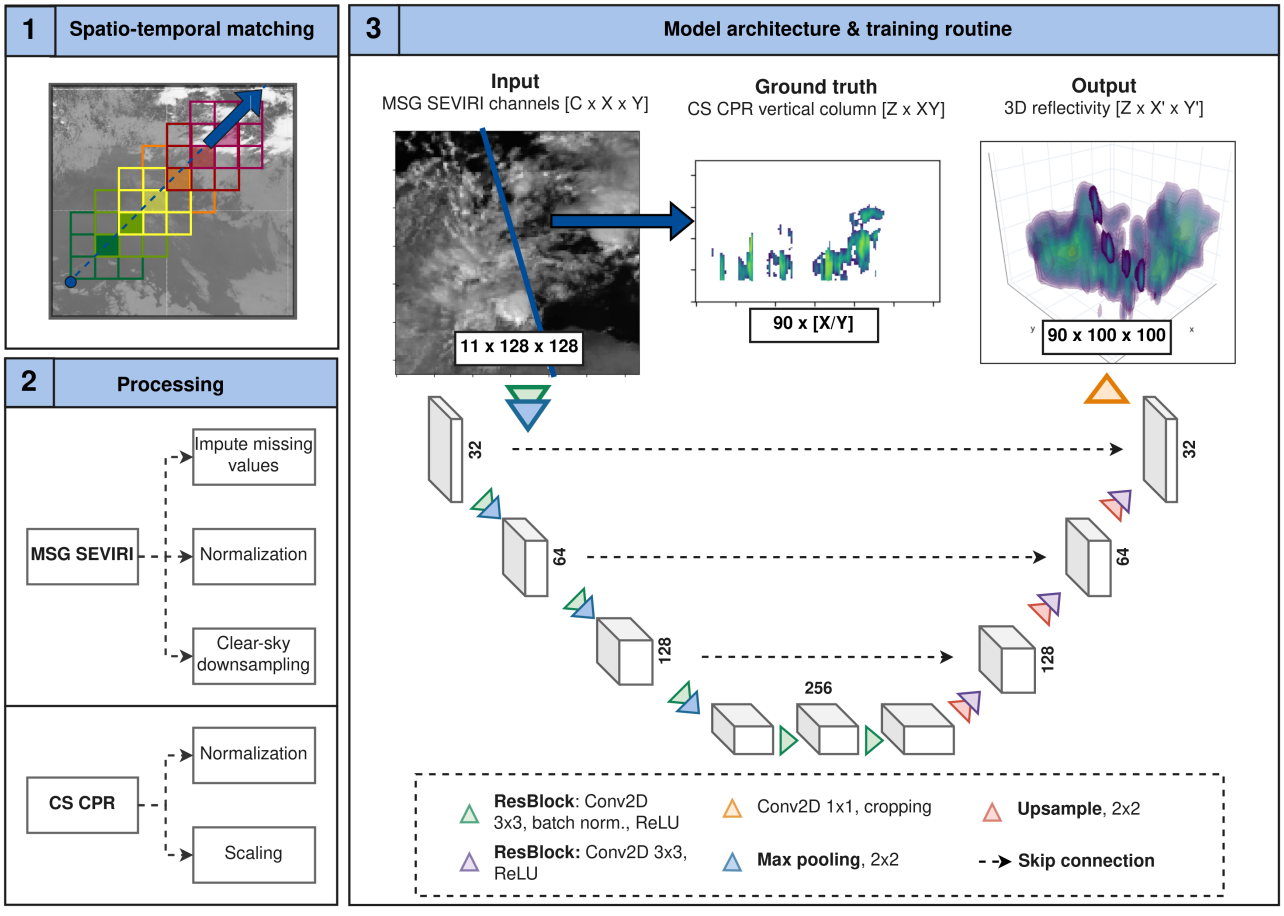

Figure 1. Workflow of the study. Part **(1)** points out the moving-window approach used for matching the radar and the satellite data. Steps needed for the processing of both datasets is depicted in **(2)**. In **(3)**, the architecture of the proposed Res-UNet is pictured alongside the input data, ground truth and predicted output. In the output sample, the location of the radar is pictured with full opacity. Each numbered box refers to the feature channels at the given model depth.

https://doi.org/10.5194/egusphere-2023-1834
Preprint. Discussion started: 16 August 2023

2.1.4 Processing

Extracted satellite samples display the physical predictors fed into the network to reconstruct the vertical cloud distribution. Using a whole year of data (2017) integrates seasonal variations into the modeling routine, leading to 30.000 samples. From these, 75 % went into training the model and 25 % into its evaluation. Since the radar data distribution is highly skewed towards clear-sky samples, reducing the percentage of cloud-free ground truth in the final dataset to 10 % tackles this imbalance (Jeppesen et al., 2019). This threshold accounts for the classification of whole samples, not the proportion within single images. Nevertheless, a cloudy scene can still consist of a big proportion of background pixels (Fig. 1). Data from each satellite channel x was normalized between [-1,1] by

$$x' = \frac{x - \mu}{\sigma} \tag{1}$$

using the arithmetic mean μ and standard deviation σ of the training data (Leinonen et al., 2019). The technical limitations of the sensor require rescaling all radar tracks between 20 dBZ and -25 dBZ. Reducing the data to 90 height levels between 2.4 and 24 km minimizes the influence of the topography and higher atmosphere. Otherwise, the high attenuation degrades the quality flag of the CloudSat radar in high and low altitudes. Smoothing the CloudSat values by its internal quality flag diminishes noise within the samples (Marchand et al., 2008). Here, pixels lower than six were classified as missing values and set to a background value of -25 dBZ. After the quality assessment, all radar reflectivity values Z_{dB} were normalized to [-1,1] as follows

$$Z'_{dB} = 2\frac{Z_{dB} + 35dB}{55dB} + 1 \tag{2}$$

by the maximum and minimum [-35, 20] of the value range (Stephens et al., 2008; Leinonen et al., 2019).

2.2 Model architecture and training

The backbone of the study rests upon the Res-UNet architecture (LeCun et al., 2015; Ronneberger et al., 2015). While the UNet is well established for tasks from vision computing, evaluating its feasibility for environmental data is still in progress (Dixit et al., 2021). The Res-UNet displays a modified framework designed for the use-case of remote sensing data. By adding residual connections and continuous pooling operations, the dependence of the network on the input's location is reduced (Diakogiannis et al., 2020). Former studies dealing with the classification of tree species (Cao and Zhang, 2020), the segmentation of buildings (Dixit et al., 2021), or the delineation of precipitation intensity (Zhang et al., 2023) emphasize the potential of the Res-UNet to adequately address the importance of spatial coherence in a dynamic environment (Marais et al., 2020). In this study, the regression derives cloud reflectivities in dBZ for each pixel in a three-dimensional image field (Hilburn et al., 2020; Leinonen et al., 2019; Zhang et al., 2023). By seeking non-linear approximations of between the input and the output data, the neural network can detect complex relationships between the variables (Lee et al., 2021).

https://doi.org/10.5194/egusphere-2023-1834
Preprint. Discussion started: 16 August 2023

As introduced by Ronneberger et al. (2015), the UNet and its modifications provide an almost symmetrical architecture. Figure 1 illustrates the network architecture whereas each convolution is expanded by the structure of a residual block as described by Diakogiannis et al. (2020). Following a sequence of down-sampling layers on the encoder side, the original spatial extent of 128 x 128 pixels is reconstructed by continuous up-sampling layers in the decoder side (Lee et al., 2021). To maintain the spatial coherence in the last down-sampling layer, the model depth is restricted to 4 subsequent convolutions. Each residual block consists of a convolution with a kernel size of 3 x 3 and shortcut connections used to avoid model degradation (Diakogiannis et al., 2020). A batch normalization layer and an activation layer with a rectified linear unit (ReLU) follow the convolution of the input layer for improved robustness and to avoid extreme values (Le Goff et al., 2017; Li et al., 2018). A maximum pooling of size 2 x 2 reduces the initial spatial extent from 128 x 128 to 64 x 64 pixels (Lee et al., 2021). Repeating this routine of operations for every layer in the encoder, we halve the image size every time while doubling the number of feature channels leading to a final size of 256 x 8 x 8 pixels (Ronneberger et al., 2015). After the last pooling layer, we apply a sequence of repeated convolutions followed by batch normalization and a ReLU activation.

On the decoder side, a likewise sequence of upsampling blocks accompanied by features originating skip connections expands the low-resolution image to its original extent but with a modified representation (Li et al., 2018). In this case, these are the 3D radar reflectivities. The upsampling displays the inversion of the pooling on the encoder side, doubling the spatial extent to fit the size of the corresponding skip connection. In each step, the upsampling is followed by a residual block with a convolution and a ReLU activation layer ((Lee et al., 2021)). After the last upsampling block, a convolution with a kernel size of 1 x 1 maps the output to a size of 90 x 128 x 128 pixels. A subsequent removal of the outermost pixels leads to a final size of 90 x 100 x 100 pixels (Jeppesen et al., 2019).

Choosing the Adaptive Moment Estimation (ADAM) method ensures model optimization due to its fast convergence rate (Kingma and Ba, 2014). As flipped images are perceived as new samples, we enhance the amount of training data by giving all samples a chance of 25% to be either vertically or horizontally rotated (Jeppesen et al., 2019). Predicted reflectivities are matched to the CloudSat value range with a lower limit of -25 dBZ to differentiate a cloud signal from background noise (Leinonen et al., 2019).

2.3 Evaluation

2.3.1 Model performance

The model performance is evaluated by the root-mean-square error (RMSE), which equally penalizes misses and false alarms (Lee et al., 2021). Since ground truth is limited to the radar overpass, only 10 % of the pixels are used for the error calculation (Wang et al., 2020). The loss is calculated according to:

$$RMSE = \sqrt{\sum_{i=1}^{D}(x_i - y_i)^2}. \tag{3}$$

https://doi.org/10.5194/egusphere-2023-1834
Preprint. Discussion started: 16 August 2023

The results of the DL network are compared against two pixel-based methods to examine its performance along the radar track. Training data for these approaches is extracted from the previously created dataset. For each image, the horizontal diagonal of the radar overpass is divided into pixel-wise training samples along the XY–axis. The final input consists of an array of 11 satellite channels. Each ground truth sample displays an array of 90 height bins along the Z–axis (Fig. 1). Preserving the index of the pixel along the diagonal during the training routine allows a reconstruction of the radar track. Both models utilize the normalized satellite data to reconstruct the radar reflectivity (Sect. 2.1.4). The RMSE is calculated after rescaling the output back to the dBZ scale. First, this study applies an ordinary least squares model with multiple regression output (OLS) as a baseline model (Miller et al., 2014). In this case, all 11 satellite channels were used as independent predictor variables to estimate the radar reflectivity for each pixel along the cloud column. Second, a Random-Forest (RF) regression is applied (Wang et al., 2021). As a supervised ML algorithm, the RF pictures a robust method when working with large environmental datasets in the natural sciences (Boulesteix et al., 2012). In the past, numerous studies investigated its feasibility for complex meteorological data, e.g., detecting clouds (McCandless and Jiménez, 2020) or delineating rain rates (Kühnlein et al., 2014). This study tested a minimal setup with 100 trees, each choosing a random subset of predictors (McCandless and Jiménez, 2020). Both models use the same data split as the Res-UNet (Sect. 2.1.4). After training, the original radar track is restored to enable a track-wise comparison.

2.3.2 Comprehensive predictions

A 3D cloud tomography can be achieved by dividing the satellite FD into 128 x 128 pixel subsets. These images are individually processed and fed into the network. Combining their outputs of 100 x 100 pixels into a joined 3D prediction of 2400 x 2400 pixels enables a whole satellite grid coverage. This comprehensive cloud tomography is derived for every time step of the satellite dataset and is used to evaluate the network's ability to create a smooth interpolation of large-scale cloud fields.

2.3.3 Cloud top properties

Since neither simulations nor observational-based models deliver comparable data, the predictions are interpreted based on their applicability for deriving cloud-top properties (Wang et al., 2023). At first, CloudSat data and track-wise predictions are used to compute the cloud top height (CTH) for the validation data. The CTH is defined as the distance between the ground surface and the uppermost cloud layer for every vertical column (Huo et al., 2020). This calculation requires converting the CloudSat height bins into a kilometer scale. Values with a reflectivity higher than -15 dBZ display a cloudy signal, whereas lower values are classified as the background class (Marchand et al., 2008). The final output displays an aggregation on a monthly scale. Afterward, the CTH of the FD 3D reflectivities is compared to the operational product CLAAS-V002E1 (CLoud property dAtAset using SEVIRI, Edition 2) (Finkensieper et al., 2020). Based on the MSG SEVIRI channels and additional model data, CLAAS-V002E1 provides information on the macrophysical and microphysical cloud properties. It is available as a monthly aggregate with a resolution of 0.05 ° on the MSG SEVIRI FD. The goal is to rate the predicted CTH compared to CLAAS-V002E1 by pointing out the overall agreement and regional differences.

https://doi.org/10.5194/egusphere-2023-1834
Preprint. Discussion started: 16 August 2023

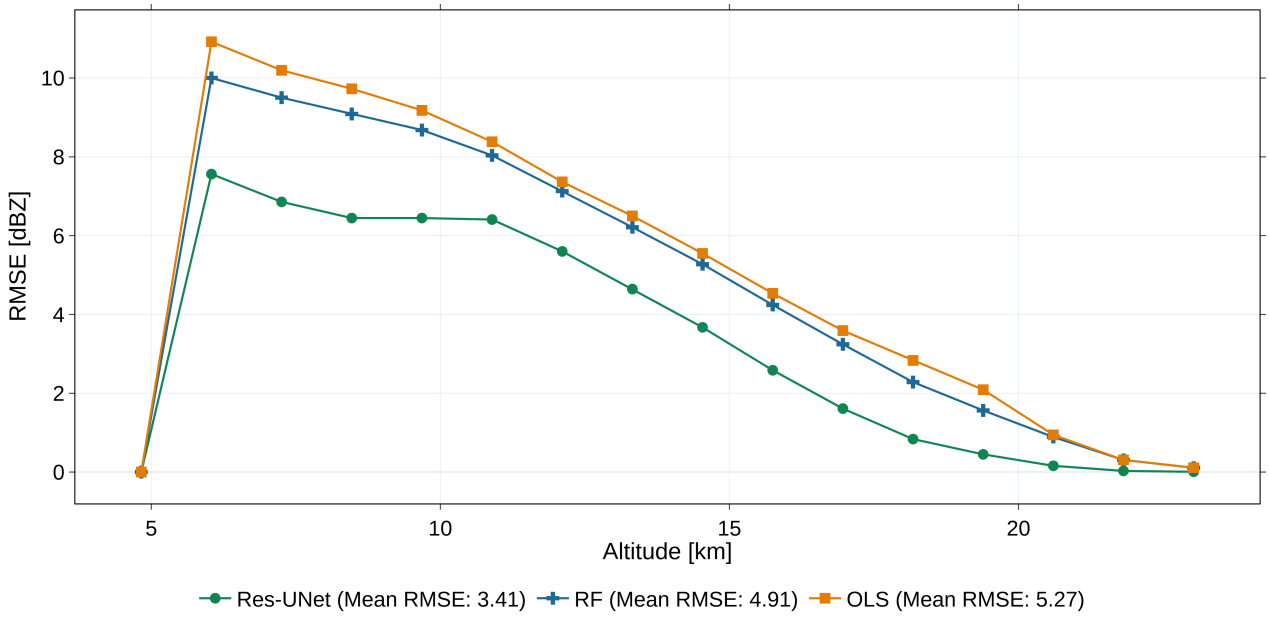

Figure 2. Comparison of the height dependent RMSE for every height bin between 5–24 km and the mean error for all models calculated on the validation dataset.

3 Results

3.1 Evaluating the model performance

Three models were trained to compare the performance of the different approaches (Sect. 2.3.1). Due to the applied CloudSat quality flag, predictions below 5 km are influenced by the high amount of background values at -25 dBZ (Sect. 2.1.4). As a consequence, the following evaluation refers to the predicted reflectivity above 5 km. The results illustrate a substantial improvement when applying a DL framework compared to the OLS and RF. Figure 2 illustrates the variance of the error between 5–24 km. The mean RMSE varies between 3.41 dBZ for the Res-UNet and 4.91 dBZ (RF) or 5.27 dBZ (OLS). This difference depicts a reduction of the total error from 11.7 % (OLS) or 10.9 % (RF) to 7.5 % for the DL network. The overall RMSE and the difference between the models reach their maximum in low altitudes between 5–7 km height. In higher altitudes with more uniform clouds, the performance of all models improves. Nevertheless, the DL network outperforms the other approaches at every height level (Fig. 2).

To evaluate the accuracy of the models on different height levels, the normalized difference between the observed and predicted reflectivities is analyzed by a two-dimensional joint distribution plot (Steiner et al., 1995). All models deviate from the original radar data, especially in low altitudes (Fig. 3). The differences get smaller in higher parts of the troposphere and tropopause. A diagonal of high agreement with the observed data from high altitudes with low reflectivities to lower altitudes

https://doi.org/10.5194/egusphere-2023-1834
Preprint. Discussion started: 16 August 2023

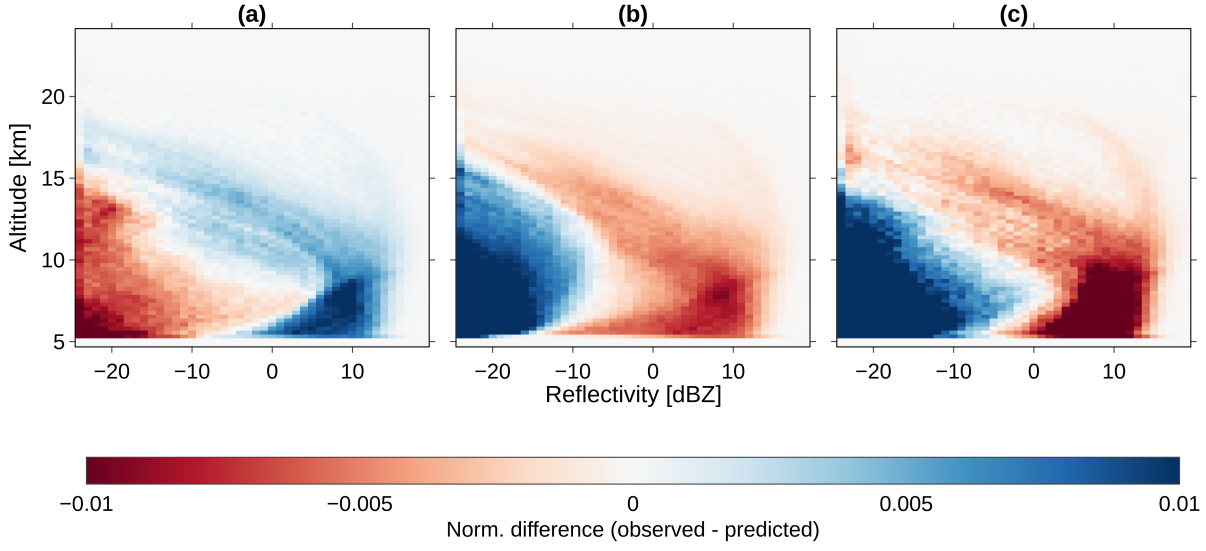

Figure 3. Joint plot of the normalized difference between the observed and predicted reflectivity. The deviation on each height bin between 5–24 km is compared for the Res-UNet **(a)**, the ordinary least squares model (OLS) **(b)**, and the Random-Forest regression (RF) **(c)**.

with higher reflectivities can be observed with the steepest diversion for the OLS. Appearing in the shape of two contrasting parts, the direction differs between the Res-UNet and the other models. That said, the DL network indicates an underestimation of high reflectivities and an overestimation of low reflectivities for low-level clouds. Predictions in higher altitudes represent a smaller deviation from the ground truth. The other models show an overestimation of high reflectivities and an underestimation of low values in both, low- and mid-altitude. In terms of total deviation from the ground truth, the Res-UNet performs best out of the three proposed models.

3.2 Analysis of cloud vertical properties

Figure 4 depicts the model predictions and the observed CloudSat reflectivities along the radar track for four samples. All models detect the horizontal location of different clouds along the XY–axis. A detailed view of the individual radar tracks illustrates the transferability of the proposed DL method. In contrast to the RF and OLS, the Res-UNet reconstructs the clouds along the original track more adequately with a RMSE between 4.1–6.9 dBZ (Fig. 4). Especially for clouds with a less uniform shape, it represents the small-scale variability with higher accuracy. In the core regions of the cloud, the underestimation of high reflectivities is demonstrated. A denominational structure within each cloud is apparent for the RF and OLS. Contrasting, the output of the Res-UNet pictures more interconnected and smooth features. The OLS and RF fail to predict shallow clouds

https://doi.org/10.5194/egusphere-2023-1834
Preprint. Discussion started: 16 August 2023

at high altitudes and complex structures of multi-layered clouds. Here, the Res-UNet shows more robust results leading to a more accurate reconstruction of the CloudSat data.

Due to the applied quality flag, few clouds are detected below 5 km, thus, no RMSE is calculated here (Fig. 2). After a stage of adjustment, more pixels pass the quality criterion above this level. An enhanced RMSE of 8 dBZ for the Res-UNet accompanies this sudden augmentation of available data points. Further increasing altitudes correspond to a decreasing RMSE. More uniform clouds above 15 km, like extended tropical cirrus, are easier to predict. In turn, this leads to a lower model uncertainty (Fig. 2, Fig. 3). That said, the results display a trade-off between generating noise-free images and minimizing the amount of skipped data points. While the model accurately identifies single-layer clouds and their horizontal location along the radar track, it misses the sharp edges of multi-layer clouds, especially in mid-altitudes. Most clear-sky situations are recognized with an almost noise-free background. The overall shape and increased intensification towards the cloud's core follow the radar, even though edges are blurred, and reflectivities remain underestimated (Fig. 4).

https://doi.org/10.5194/egusphere-2023-1834
Preprint. Discussion started: 16 August 2023

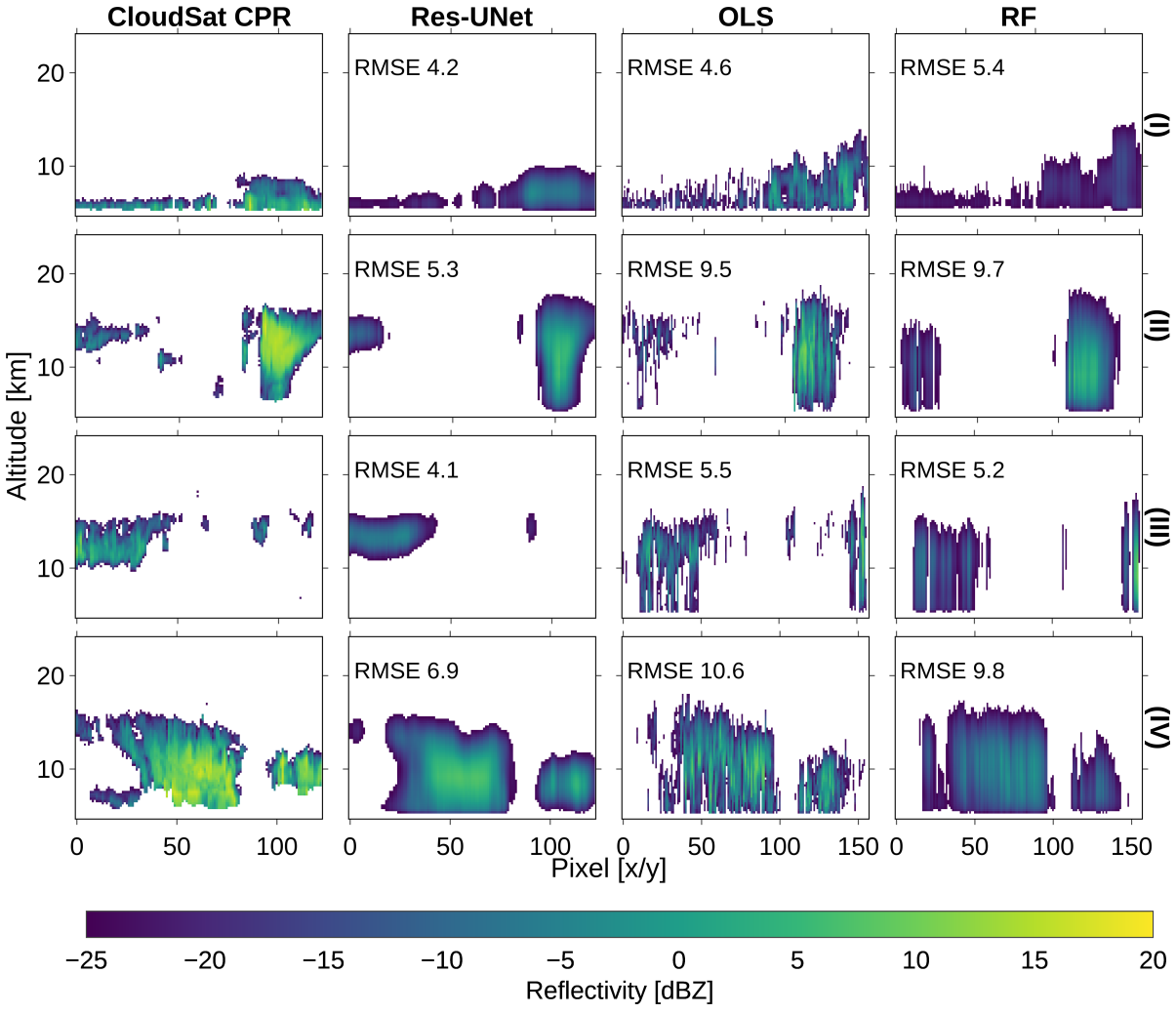

Figure 4. Reconstructing the vertical radar track along the horizontal diagonal XY–axis. Values lower than -25 dBZ are displayed transparent. For each sample **(I)**–**(IV)** the reflectivity is compared between the processed CloudSat CPR track and the predictions of the Res-UNet, the OLS, and the RF.

https://doi.org/10.5194/egusphere-2023-1834
Preprint. Discussion started: 16 August 2023

3.3 Implications and sample applications

The trained Res-UNet was used to evaluate the pixel-based vertical columns and predict clouds on the whole image domain. Results contain a 3D representation within each output image along 90 height bins. Even though observational data is missing for most pixels, smooth cloud structures can be derived in different proximity to the track (Fig. 5). These 3D images are the basis to create comprehensive predictions on the MSG SEVIRI FD. For that purpose, the satellite scene was divided into small subsets of overlapping 128 x 128 pixel images as described in Section 2.3.2. After feeding each subset into the network, the output samples of 90 x 100 x 100 pixels were merged into a scene of 90 x 2400 x 2400 pixels for the whole AOI. The results of the column's maximum reflectivity demonstrate the absence of hard borders but point out a fluent transition between image edges that enable the identification of large-scale cloud patterns. The diversity of cloud types depicted within the samples in Figure 5 illustrates the transferability of the approach to different locations and their environmental conditions. High clouds, convective complexes, and isolated cores are represented as smooth structures at the FD scale regardless their location.

Following the 3D representation, the CTH was derived from the CloudSat reflectivities and the Res-UNet predictions. Considering the available data points for the calculated CTH, predicted images surpass the radar observations by 10.000. Comparing the distributions in Figure 6 shows lower reflectivities for predicted than for observational data. Again, the high proportion of background values around -25 dBZ rests upon the imbalance within the radar data. Both datasets provide more similar results concerning the frequencies above -15 dBZ. This distinction emphasizes an overall surplus of background values in the FD prediction. Both datasets display a maximum CTH at up to 7 km height. This first peak is overestimated by the model. The absence of a second peak around 12–15 km height is reflected within the normalized difference. Here, the model shifts towards lower altitudes than the observational data (Fig. 6). The underestimated second peak can be traced back to high clouds with a low optical thickness, which is sometimes not well recognized, especially in the visible channels of MSG SEVIRI. These channels are identified as essential information providers for the ML algorithm, and therefore those high clouds are also underestimated in the derived radar reflectivities.

Although the total accuracy is improvable, derived data and deducted parameters allow an expedient investigation of regional differences. Comparing the model output and the CTH from the CLAAS-V002E1 product (Finkensieper et al., 2020) reveals an overall high agreement. Regional differences arise around the equator and mid to high latitudes. Regarding the first, the model is biased toward predicting lower clouds. In the latter regions, they appear too intense, especially over water bodies of the southern hemisphere (Fig. 7). Unlike most satellite-based procedures, the CTH is derived without integrating additional data, such as vertical temperature profiles from e.g., model forecast or re-analysis data. This simplification reduces the workload for users and the co-dependence of corresponding data. Therefore, the approach offers added value in terms of a more efficient investigation of cloud-related processes.

https://doi.org/10.5194/egusphere-2023-1834
Preprint. Discussion started: 16 August 2023

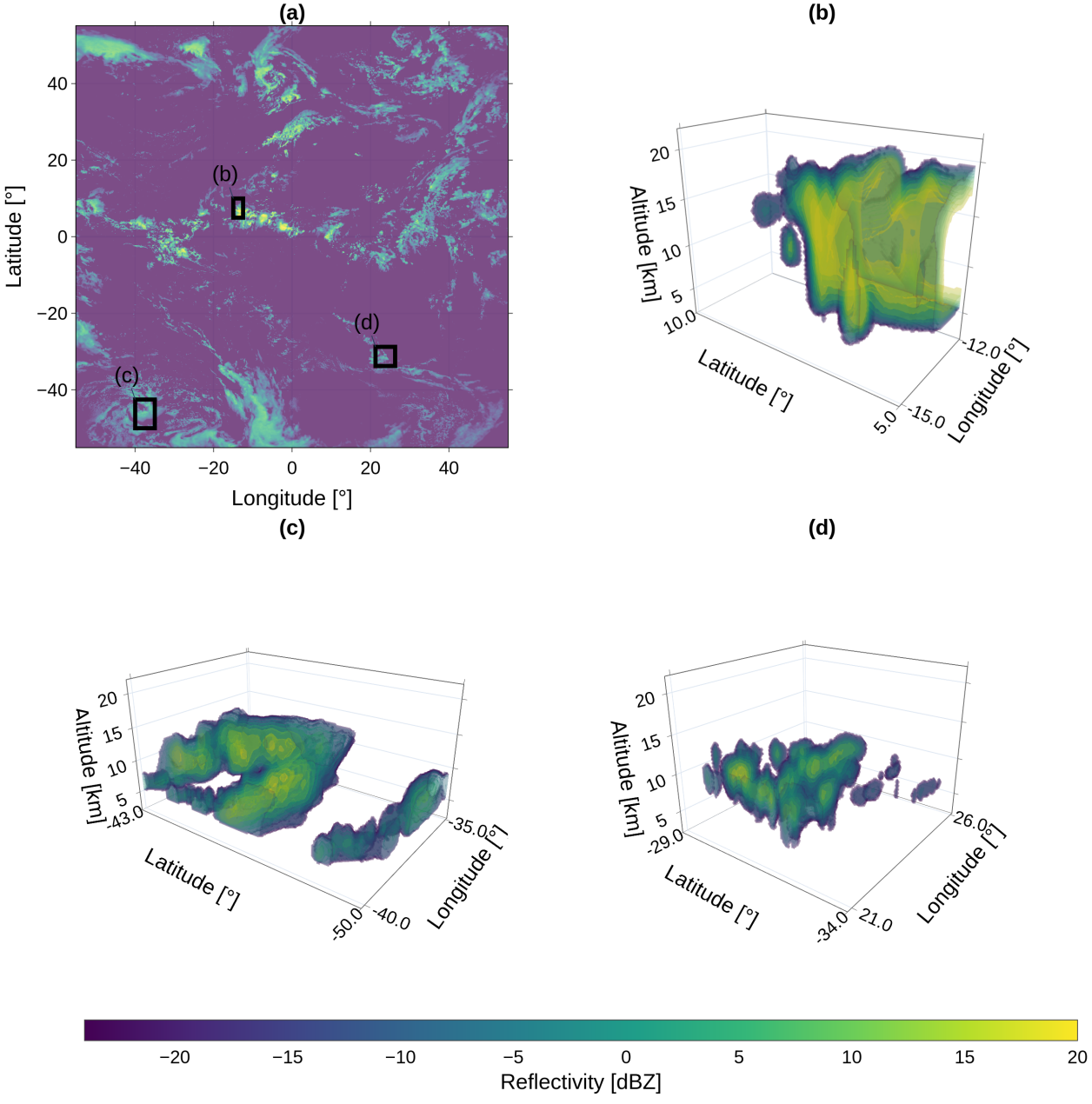

Figure 5. Prediction of 3D cloud structures for the FD MSG SEVIRI domain with a a top-view on the maximum cloud column reflectivity for each pixel on 06 May 2016, 13:00 UTC **(a)**. The detailed views in **(b)**, **(c)**, and **(d)** show the cloud tomography at different locations of the FD.

https://doi.org/10.5194/egusphere-2023-1834
Preprint. Discussion started: 16 August 2023

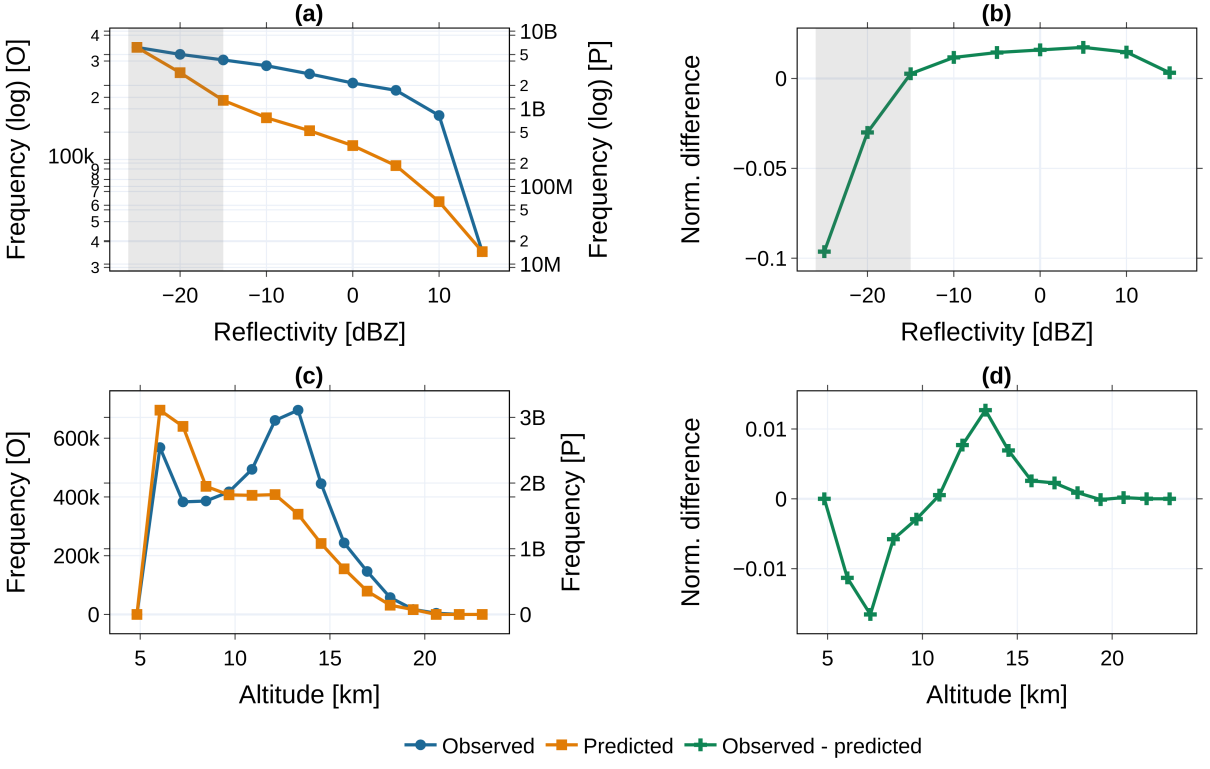

Figure 6. Comparing the FD distribution of reflectivities and CTH derived from CloudSat and the model aggregated for May, 2016. The upper row frequencies **(a)** and **(b)** display the dBZ for observed and predicted data and their normalized difference. Grey areas lie below the threshold of -15 dBZ applied for the CTH analysis. Lower row images **(c)** and **(d)** picture the frequency of the CTH per height level (for observations above -15 dBZ) alongside the normalized difference between 5–24 km height.

https://doi.org/10.5194/egusphere-2023-1834
Preprint. Discussion started: 16 August 2023

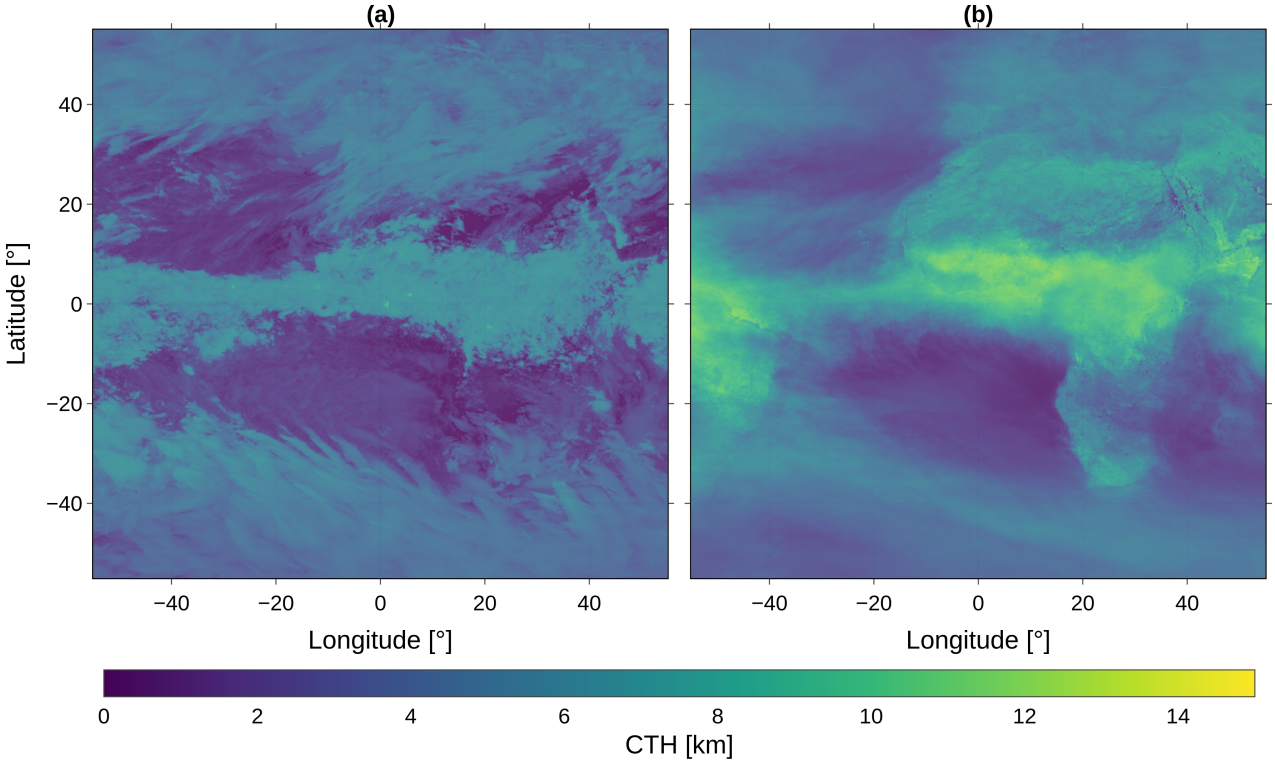

Figure 7. Aggregated CTH derived from the Res-UNet **(a)** and from the CLAAS-V002E1 CTO product **(b)** for May, 2016.

https://doi.org/10.5194/egusphere-2023-1834
Preprint. Discussion started: 16 August 2023

4 Discussion

In contrast to established ML methods like RF which need a cumbersome selection of predictor variables, the network in this study learns directly from the data (Kühnlein et al., 2014; Leinonen et al., 2019). That said, the DL approach reduces the time spent on processing and the user-generated bias (Jeppesen et al., 2019; Jiao et al., 2020). Standard DL models often use gray-scale or RGB images (Drönner et al., 2018). In contrast, the input data in our study consists of multiple satellite channels. That is why using a pre-trained model is restrained by expensive modifications (Amato et al., 2020). To evaluate the feasibility of the approach, we test a minimal architecture for transferring the 2D resolved satellite data to a 3D perspective.

While Hilburn et al. (2020) were able to reconstruct the radar signal over the USA, they are limited to a planar representation and leave out cloud development over the sea surface. Contrasting their and others work, our study integrates a heterogeneous landscape into the training routine (Leinonen et al., 2019; Le Goff et al., 2017; Hilburn et al., 2020; Forster et al., 2021). The latitude and topography are highly influential for cloud microphysics (Wang et al., 2023). Nonetheless, defining those variables as additional predictors has a negligible effect on the model performance. Instead, the network performs equally well over land and ocean bodies capturing the shape of convective and shallow clouds. Predictions at nighttime are limited due to the influence of solar radiation in the channels located within wavelengths of the visible spectrum (Hilburn et al., 2020; Jeppesen et al., 2019). Leaving out the affected channels downgrades the overall performance. While the results imply a high agreement between observations and predictions, distortions are possible. Since the satellite data deliver only information on the uppermost layer, the incoming signal could originate from any surface with an enhanced albedo (Drönner et al., 2018).

The Res-UNet in this study generates its predictions with the influence of the neighboring pixels along the image domain. In contrast to pixel-based DL methods like the CNN or CGAN, the Res-UNet utilizes a larger receptive field preserving the spatial dimensionality and global context information during the training routine (Wang et al., 2022). Thus, it receives a more accurate spatial connectivity between the pixels and following, the clouds within the image. While the OLS and RF solely get information on the reflectivities along a single cloud column, the Res-UNet enables an interpolation towards an FD perspective. While the CGAN was restrictively trained over sea surfaces, the influence of the variability of the topography beneath needs to be included (Wang et al., 2023). The restoration of the original track is comparable to results achieved by Leinonen et al. (2019) and Wang et al. (2023). The RMSE varies between 0–1 dBZ for cloud-free samples, 3–7 dBZ for more uniform clouds, and more than 10 dBZ for multi-layer clouds (Leinonen et al., 2019). All networks struggle to depict multi-layer structures accurately. Due to the sensor limitations of CloudSat, few signals close to the ground are received (Stephens et al., 2008). In consequence, predictions at low altitudes are error-prone. This issue is reflected within the normalized differences between observed and predicted reflectivities (Fig. 2). Similar results are achieved by Leinonen et al. (2019) where falsely estimated reflectivities appear in similar dBZ regions up to 12 km height. In both cases, an underestimation of high reflectivities is predominant. Since the input data of the CGAN originates from the MODIS satellite, it has a higher native resolution than the MSG SEVIRI data enabling sharper predictions along the track. On the other hand, the mismatch between CloudSat and MSG SEVIRI requires an aggregation of each radar pixel leading to reduced contrasts and blurry edges within individual clouds. Nevertheless, polar-orbiting satellites like MODIS lack spatio-temporal coverage compared to geostationary satellites

https://doi.org/10.5194/egusphere-2023-1834
Preprint. Discussion started: 16 August 2023

(Dubovik et al., 2021). By using MSG SEVIRI data, the amount of training data substantially increases. Matching MODIS with CloudSat accounts for about 24.000 training samples for six years (Wang et al., 2023). This study extracted about 30.000 training samples for only one year, equaling a ratio of about 1:7 for the whole period.

A compromise on the resolution is necessary to obtain predictions on the FD. However, newly emerging instruments offer an enticing prospect to tackle this information loss. The recently launched satellite Meteosat Third Generation by EUMETSAT (Holmlund et al., 2021) provides data in a resolution of 1 km. This sensor allows a more accurate representation of individual clouds. While the approach is currently restricted to a domain of 60° in all directions, assimilating related geostationary satellites helps to achieve global coverage. Consequently, this model can be used to close current gaps in the 3D representation of clouds, leading to a seamless coverage of the vertical column along the troposphere for the first time.

5 Conclusions

With the help of a neural network, this study demonstrates the potential to infer a comprehensive 3D perspective of radar reflectivities from 2D geostationary satellite data for the first time. While former studies are restricted to a regional extent or the flight path of the ground truth instrument, this approach provides a flexible and landscape-independent framework to model the cloud signal with a high spatio-temporal resolution. Since it is independent of external or interconnected data sources, the bias within the data is reduced. Overall, the approach leads to an accurate representation of multi-scale dynamics in varying environmental conditions. Although the results are affected by sensor-specific limitations, a vast potential for applications in the field of weather and climate is apparent. With steadily growing data and the emergence of improved instruments, the results can close the consisting global data gap, especially in secluded regions and above the sea surface. Future work will focus on extending the proposed network by data with an enhanced spatial and temporal resolution and investigating 3D cloud processes in proceeding applications.

Code and data availability. The source code for the satellite data matching scheme and model framework are available upon request to the corresponding author and will be published with acceptance. Meteosat SEVIRI image data used in this study have been downloaded at https://navigator.eumetsat.int/product/EO-:EUM:DAT:MSG:HRSEVIRI (EUMETSAT Data Services, 2023). The level 2B-GEOPROF CloudSat data have been downloaded at http://-www.cloudsat.cira.colostate.edu/ (CloudSat Data Processing Center, 2023). The CLAAS-2.1 data were obtained from https://doi.org/10.56-76/EUM_SAF_CM/CLAAS/V002 (Finkensieper et al., 2020).

Author contributions. S.B and H.T. designed the study. S.B and S.N. developed the model code. S.B performed the modeling and visualization. S.B. and H.T. contributed to the model validation and analysis of cloud properties. S.B. and H.T. wrote the draft of the paper. All authors have read and agreed to the published version of the manuscript.

https://doi.org/10.5194/egusphere-2023-1834
Preprint. Discussion started: 16 August 2023

Competing interests. The authors declare that they have no conflict of interest.

Acknowledgements. The study is supported by the project "Big Data in Atmospheric Physics (BINARY)", funded by the Carl Zeiss Foundation (grant P2018-02-003). We acknowledge the infrastructure provided by the Max Planck Graduate Center Mainz. We acknowledge EUMETSAT for providing access to the Meteosat SEVIRI image data. We acknowledge the Cooperative Institute for Research in the Atmosphere, CSU, for providing access to the CloudSat 2B-GEOPROF data. We acknowledge CM SAF for providing access to the CLAAS-2.1 data. We thank P. Spichtinger for useful discussions and comments on the manuscript.

https://doi.org/10.5194/egusphere-2023-1834
Preprint. Discussion started: 16 August 2023

References

Amato, F., Guignard, F., Robert, S., and Kanevski, M.: A novel framework for spatio-temporal prediction of environmental data using deep learning, Sci. Rep., 10, https://doi.org/10.1038/s41598-020-79148-7, 2020.

Barker, H. W., Jerg, M. P., Wehr, T., Kato, S., Donovan, D. P., and Hogan, R. J.: A 3D cloud-construction algorithm for the EarthCARE satellite mission, Q. J. R. Meteorol., 137, 1042–1058, https://doi.org/10.1002/qj.824, 2011.

Bedka, K., Brunner, J., Dworak, R., Feltz, W., Otkin, J., and Greenwald, T.: Objective Satellite-Based Detection of Overshooting Tops Using Infrared Window Channel Brightness Temperature Gradients, JAMC, 49, 181–202, https://doi.org/10.1175/2009JAMC2286.1, 2010.

Benas, N., Finkensieper, S., Stengel, M., van Zadelhoff, G.-J., Hanschmann, T., Hollmann, R., and Meirink, J. F.: The MSG-SEVIRI-based cloud property data record CLAAS-2, ESSD, 9, 415–434, https://doi.org/10.5194/essd-9-415-2017, 2017.

Bocquet, M., Elbern, H., Eskes, H., Hirtl, M., Žabkar, R., Carmichael, G. R., Flemming, J., Inness, A., Pagowski, M., Pérez Camaño, J. L., Saide, P. E., San Jose, R., Sofiev, M., Vira, J., Baklanov, A., Carnevale, C., Grell, G., and Seigneur, C.: Data assimilation in atmospheric chemistry models: current status and future prospects for coupled chemistry meteorology models, Atmos. Chem. Phys., 15, 5325–5358, https://doi.org/10.5194/acp-15-5325-2015, 2015.

Bony, S., Stevens, B., Frierson, D. M. W., Jakob, C., Kageyama, M., Pincus, R., Shepherd, T. G., Sherwood, S. C., Siebesma, A. P., Sobel, A. H., Watanabe, M., and Webb, M. J.: Clouds, circulation and climate sensitivity, Nat. Geosci., 8, 261–268, https://doi.org/10.1038/ngeo2398, 2015.

Boulesteix, A.-L., Janitza, S., Kruppa, J., and König, I. R.: Overview of random forest methodology and practical guidance with emphasis on computational biology and bioinformatics, WIREs Data Min. Knowl. Discov., 2, 493–507, https://doi.org/https://doi.org/10.1002/widm.1072, 2012.

Cao, K. and Zhang, X.: An Improved Res-UNet Model for Tree Species Classification Using Airborne High-Resolution Images, Remote Sens., 12, https://doi.org/10.3390/rs12071128, 2020.

Cintineo, J. L., Pavolonis, M. J., Sieglaff, J. M., Wimmers, A., Brunner, J., and Bellon, W.: A Deep-Learning Model for Automated Detection of Intense Midlatitude Convection Using Geostationary Satellite Images, Weather and Forecast., 35, 2567 – 2588, https://doi.org/https://doi.org/10.1175/WAF-D-20-0028.1, 2020.

CloudSat Data Processing Center: Data Products, CloudSat DPC [data set], https://www.cloudsat.cira.colostate.edu/data-products, accessed: 2023-07-27, 2023.

Denby, L.: Discovering the Importance of Mesoscale Cloud Organization Through Unsupervised Classification, Geophys. Res. Lett., 47, https://doi.org/10.1029/2019GL085190, 2020.

Diakogiannis, F. I., Waldner, F., Caccetta, P., and Wu, C.: ResUNet-a: A deep learning framework for semantic segmentation of remotely sensed data, ISPRS J. Photogramm. Remote Sens., 162, 94–114, https://doi.org/10.1016/j.isprsjprs.2020.01.013, 2020.

Dixit, M., Chaurasia, K., and Kumar Mishra, V.: Dilated-ResUnet: A novel deep learning architecture for building extraction from medium resolution multi-spectral satellite imagery, Expert Syst. Appl., 184, 115 530, https://doi.org/10.1016/j.eswa.2021.115530, 2021.

Drönner, J., Korfhage, N., Egli, S., Mühling, M., Thies, B., Bendix, J., Freisleben, B., and Seeger, B.: Fast Cloud Segmentation Using Convolutional Neural Networks, Remote Sens., 10, 1782, https://doi.org/10.3390/rs10111782, 2018.

Dubovik, O., Schuster, G., Xu, F., Hu, Y., Bösch, H., Landgraf, J., and Li, Z.: Grand Challenges in Satellite Remote Sensing, Front. Remote Sens., 2, 619 818, https://doi.org/10.3389/frsen.2021.619818, 2021.

https://doi.org/10.5194/egusphere-2023-1834
Preprint. Discussion started: 16 August 2023

EUMETSAT Data Services: High Rate SEVIRI Level 1.5 Image Data - MSG - 0 degree, https://navigator.eumetsat.int/product/EO:EUM:DAT:MSG:HRSEVIRI, accessed: 2023-07-27, 2023.

Finkensieper, S., Meirink, J. F., van Zadelhoff, G.-J., Hanschmann, T., Benas, N., Stengel, M., Fuchs, P., Hollmann, R., Kaiser, J., and Werscheck, M.: CLAAS-2.1: CM SAF CLoud property dAtAset using SEVIRI - Edition 2.1, https://doi.org/10.5676/EUM_SAF_CM/CLAAS/V002_01, 2020.

Forster, L., Davis, A. B., Diner, D. J., and Mayer, B.: Toward Cloud Tomography from Space Using MISR and MODIS: Locating the "Veiled Core" in Opaque Convective Clouds, J. Atmos. Sci., 78, 155–166, https://doi.org/10.1175/JAS-D-19-0262.1, 2021.

Guillaume, A., Kahn, B. H., Yue, Q., Fetzer, E. J., Wong, S., Manipon, G. J., Hua, H., and Wilson, B. D.: Horizontal and Vertical Scaling of Cloud Geometry Inferred from CloudSat Data, J. Atmos. Sci., 75, 2187–2197, https://doi.org/10.1175/JAS-D-17-0111.1, 2018.

Ham, S.-H., Kato, S., Barker, H. W., Rose, F. G., and Sun-Mack, S.: Improving the modelling of short-wave radiation through the use of a 3D scene construction algorithm, Q. J. R. Meteorol., 141, 1870–1883, https://doi.org/https://doi.org/10.1002/qj.2491, 2015.

Han, L., Liang, H., Chen, H., Zhang, W., and Ge, Y.: Convective Precipitation Nowcasting Using U-Net Model, IEEE Trans. Geosci. Remote Sens., 60, 1–8, https://doi.org/10.1109/TGRS.2021.3100847, 2022.

Hilburn, K. A., Ebert-Uphoff, I., and Miller, S. D.: Development and Interpretation of a Neural-Network-Based Synthetic Radar Reflectivity Estimator Using GOES-R Satellite Observations, J. Appl. Meteorol. Climatol., 60, 3–21, https://doi.org/10.1175/JAMC-D-20-0084.1, 2020.

Holmlund, K., Grandell, J., Schmetz, J., Stuhlmann, R., Bojkov, B., Munro, R., Lekouara, M., Coppens, D., Viticchie, B., August, T., Theodore, B., Watts, P., Dobber, M., Fowler, G., Bojinski, S., Schmid, A., Salonen, K., Tjemkes, S., Aminou, D., and Blythe, P.: Meteosat Third Generation (MTG): Continuation and Innovation of Observations from Geostationary Orbit, BAMS, 102, 990–1015, https://doi.org/10.1175/BAMS-D-19-0304.1, 2021.

Hu, K., Zhang, D., and Xia, M.: CDUNet: Cloud Detection UNet for Remote Sensing Imagery, Remote Sens., 13, https://doi.org/10.3390/rs13224533, 2021.

Huo, J., Lu, D., Duan, S., Bi, Y., and Liu, B.: Comparison of the cloud top heights retrieved from MODIS and AHI satellite data with ground-based Ka-band radar, Atmos. Meas. Tech., 13, 1–11, https://doi.org/10.5194/amt-13-1-2020, 2020.

Irrgang, C., Boers, N., Sonnewald, M., Barnes, E. A., Kadow, C., Staneva, J., and Saynisch-Wagner, J.: Towards neural Earth system modelling by integrating artificial intelligence in Earth system science, Nat. Mach. Intell., 3, 667–674, https://doi.org/10.1038/s42256-021-00374-3, 2021.

Jeppesen, J. H., Jacobsen, R. H., Inceoglu, F., and Toftegaard, T. S.: A cloud detection algorithm for satellite imagery based on deep learning, Remote Sens. Environ., 229, 247–259, https://doi.org/10.1016/j.rse.2019.03.039, 2019.

Jiao, L., Huo, L., Hu, C., and Tang, P.: Refined UNet: UNet-Based Refinement Network for Cloud and Shadow Precise Segmentation, Remote Sens., 12, https://doi.org/10.3390/rs12122001, 2020.

Jones, N.: How machine learning could help to improve climate forecasts, Nature, 548, 379–379, https://doi.org/10.1038/548379a, 2017.

Jordahl, K., Bossche, J. V. D., Fleischmann, M., Wasserman, J., McBride, J., Gerard, J., Tratner, J., Perry, M., Badaracco, A. G., Farmer, C., Hjelle, G. A., Snow, A. D., Cochran, M., Gillies, S., Culbertson, L., Bartos, M., Eubank, N., Maxalbert, Bilogur, A., Rey, S., Ren, C., Arribas-Bel, D., Wasser, L., Wolf, L. J., Journois, M., Wilson, J., Greenhall, A., Holdgraf, C., Filipe, and Leblanc, F.: geopandas/geopandas: v0.8.1, https://doi.org/10.5281/ZENODO.3946761, 2020.

Karpatne, A., Ebert-Uphoff, I., Ravela, S., Babaie, H. A., and Kumar, V.: Machine Learning for the Geosciences: Challenges and Opportunities, IEEE Trans. Knowl. Data Eng., 31, 1544–1554, https://doi.org/10.1109/TKDE.2018.2861006, 2019.

https://doi.org/10.5194/egusphere-2023-1834
Preprint. Discussion started: 16 August 2023

Kingma, D. P. and Ba, J.: Adam: A Method for Stochastic Optimization, https://doi.org/10.48550/ARXIV.1412.6980, 2014.

Kühnlein, M., Appelhans, T., Thies, B., and Nauss, T.: Improving the accuracy of rainfall rates from optical satellite sensors with machine learning — A random forests-based approach applied to MSG SEVIRI, Remote Sens. Environ., 141, 129–143, https://doi.org/https://doi.org/10.1016/j.rse.2013.10.026, 2014.

Le Goff, M., Tourneret, J.-Y., Wendt, H., Ortner, M., and Spigai, M.: Deep learning for cloud detection, in: 8th International Conference of Pattern Recognition Systems (ICPRS 2017), pp. 1–6, https://doi.org/10.1049/cp.2017.0139, 2017.

LeCun, Y., Bengio, Y., and Hinton, G.: Deep learning, Nature, 521, 436–444, https://doi.org/10.1038/nature14539, 2015.

Lee, Y., Kummerow, C. D., and Ebert-Uphoff, I.: Applying machine learning methods to detect convection using Geostationary Operational Environmental Satellite-16 (GOES-16) advanced baseline imager (ABI) data, Atmos. Meas. Tech., 14, 2699–2716, https://doi.org/10.5194/amt-14-2699-2021, 2021.

Leinonen, J., Guillaume, A., and Yuan, T.: Reconstruction of Cloud Vertical Structure With a Generative Adversarial Network, Geophys. Res. Lett., 46, 7035–7044, https://doi.org/10.1029/2019GL082532, 2019.

Li, R., Liu, W., Yang, L., Sun, S., Hu, W., Zhang, F., and Li, W.: DeepUNet: A Deep Fully Convolutional Network for Pixel-Level Sea-Land Segmentation, IEEE J. Sel. Top. Appl. Earth Obs. Remote Sens., 11, 3954–3962, https://doi.org/10.1109/JSTARS.2018.2833382, 2018.

Liu, Y., Racah, E., Prabhat, M., Correa, J., Khosrowshahi, A., Lavers, D., Kunkel, K., Wehner, M., and Collins, W.: Application of Deep Convolutional Neural Networks for Detecting Extreme Weather in Climate Datasets, https://doi.org/arXiv:1605.01156, 2016.

Marais, W. J., Holz, R. E., Reid, J. S., and Willett, R. M.: Leveraging spatial textures, through machine learning, to identify aerosols and distinct cloud types from multispectral observations, Atmos. Meas. Tech., 13, 5459–5480, https://doi.org/10.5194/amt-13-5459-2020, 2020.

Marchand, R., Mace, G. G., Ackerman, T., and Stephens, G.: Hydrometeor Detection Using Cloudsat—An Earth-Orbiting 94-GHz Cloud Radar, J. Atmos. Ocean Technol., 25, 519–533, https://doi.org/10.1175/2007JTECHA1006.1, 2008.

McCandless, T. and Jiménez, P. A.: Examining the Potential of a Random Forest Derived Cloud Mask from GOES-R Satellites to Improve Solar Irradiance Forecasting, Energies, 13, https://doi.org/10.3390/en13071671, 2020.

Miller, S. D., Forsythe, J. M., Partain, P. T., Haynes, J. M., Bankert, R. L., Sengupta, M., Mitrescu, C., Hawkins, J. D., and Haar, T. H. V.: Estimating Three-Dimensional Cloud Structure via Statistically Blended Satellite Observations, J. Appl. Meteorol. Climatol., 53, 437–455, https://doi.org/10.1175/JAMC-D-13-070.1, 2014.

Noh, Y.-J., Haynes, J. M., Miller, S. D., Seaman, C. J., Heidinger, A. K., Weinrich, J., Kulie, M. S., Niznik, M., and Daub, B. J.: A Framework for Satellite-Based 3D Cloud Data: An Overview of the VIIRS Cloud Base Height Retrieval and User Engagement for Aviation Applications, Remote Sens., 14, 5524, https://doi.org/10.3390/rs14215524, 2022.

Norris, J. R., Allen, R. J., Evan, A. T., Zelinka, M. D., O'Dell, C. W., and Klein, S. A.: Evidence for climate change in the satellite cloud record, Nature, 536, 72–75, https://doi.org/10.1038/nature18273, 2016.

Pan, X., Lu, Y., Zhao, K., Huang, H., Wang, M., and Chen, H.: Improving Nowcasting of Convective Development by Incorporating Polarimetric Radar Variables Into a Deep-Learning Model, Geophys. Res. Lett., 48, e2021GL095 302, https://doi.org/https://doi.org/10.1029/2021GL095302, 2021.

Platnick, S., Meyer, K. G., King, M. D., Wind, G., Amarasinghe, N., Marchant, B., Arnold, G. T., Zhang, Z., Hubanks, P. A., Holz, R. E., Yang, P., Ridgway, W. L., and Riedi, J.: The MODIS Cloud Optical and Microphysical Products: Collection 6 Updates and Examples From Terra and Aqua, IEEE Trans. Geosci. Remote Sens., 55, 502–525, https://doi.org/10.1109/TGRS.2016.2610522, 2017.

https://doi.org/10.5194/egusphere-2023-1834
Preprint. Discussion started: 16 August 2023

Rasp, S., Pritchard, M. S., and Gentine, P.: Deep learning to represent sub-grid processes in climate models, PNAS, 115, 9684–9689, https://doi.org/10.1073/pnas.1810286115, 2018.

Reichstein, M., Camps-Valls, G., Stevens, B., Jung, M., Denzler, J., Carvalhais, N., and Prabhat: Deep learning and process understanding for data-driven Earth system science, Nature, 566, 195–204, https://doi.org/10.1038/s41586-019-0912-1, 2019.

Rolnick, D., Donti, P. L., Kaack, L. H., Kochanski, K., Lacoste, A., Sankaran, K., Ross, A. S., Milojevic-Dupont, N., Jaques, N., Waldman-Brown, A., Luccioni, A. S., Maharaj, T., Sherwin, E. D., Mukkavilli, S. K., Kording, K. P., Gomes, C. P., Ng, A. Y., Hassabis, D., Platt, J. C., Creutzig, F., Chayes, J., and Bengio, Y.: Tackling Climate Change with Machine Learning, ACM Comput. Surv., 55, 1–96, https://doi.org/10.1145/3485128, 2022.

Ronneberger, O., Fischer, P., and Brox, T.: U-Net: Convolutional Networks for Biomedical Image Segmentation., in: Medical Image Computing and Computer-Assisted Intervention – MICCAI 2015, edited by Navab, N., Hornegger, J., Wells, W. M., and Frangi, A. F., pp. 234–241, Springer International Publishing, Cham, https://doi.org/https://doi.org/10.1007/978-3-319-24574-4_28, 2015.

Runge, J., Bathiany, S., Bollt, E., Camps-Valls, G., Coumou, D., Deyle, E., Glymour, C., Kretschmer, M., Mahecha, M. D., Muñoz-Marí, J., van Nes, E. H., Peters, J., Quax, R., Reichstein, M., Scheffer, M., Schölkopf, B., Spirtes, P., Sugihara, G., Sun, J., Zhang, K., and Zscheischler, J.: Inferring causation from time series in Earth system sciences, Nat. Commun., 10, 2553, https://doi.org/10.1038/s41467-019-10105-3, 2019.

Schmetz, J., Pili, P., Tjemkes, S., Just, D., Kerkmann, J., Rota, S., and Ratier, A.: An Introduction to Meteosat Second Generation (MSG), BAMS, 83, 977–992, https://doi.org/10.1175/1520-0477(2002)083<0977:AITMSG>2.3.CO;2, 2002.

Seiz, G. and Davies, R.: Reconstruction of cloud geometry from multi-view satellite images, Remote Sens. Environ., 100, 143–149, https://doi.org/10.1016/j.rse.2005.09.016, 2006.

Shepherd, T. G.: Atmospheric circulation as a source of uncertainty in climate change projections, Nat. Geosci., 7, 703–708, https://doi.org/10.1038/ngeo2253, 2014.

Sieglaff, J., Hartung, D., Feltz, W., Cronce, L., and Lakshmanan, V.: A Satellite-Based Convective Cloud Object Tracking and Multipurpose Data Fusion Tool with Application to Developing Convection, J. Atmos. Ocean. Technol., 30, 510–525, https://doi.org/10.1175/JTECH-D-12-00114.1, 2013.

Steiner, M., Houze, R. A., and Yuter, S. E.: Climatological Characterization of Three-Dimensional Storm Structure from Operational Radar and Rain Gauge Data, J. Climatol. Appl. Meteorol., 34, 1978–2007, https://doi.org/10.1175/1520-0450(1995)034<1978:CCOTDS>2.0.CO;2, 1995.

Stephens, G. L., Vane, D. G., Tanelli, S., Im, E., Durden, S., Rokey, M., Reinke, D., Partain, P., Mace, G. G., Austin, R., L'Ecuyer, T., Haynes, J., Lebsock, M., Suzuki, K., Waliser, D., Wu, D., Kay, J., Gettelman, A., Wang, Z., and Marchand, R.: CloudSat mission: Performance and early science after the first year of operation, J. Geophys. Res. Atmos., 113, https://doi.org/10.1029/2008JD009982, 2008.

Stevens, B. and Bony, S.: What Are Climate Models Missing?, Science, 340, 1053–1054, https://doi.org/10.1126/science.1237554, 2013.

Stubenrauch, C. J., Rossow, W. B., Kinne, S., Ackerman, S., Cesana, G., Chepfer, H., Girolamo, L. D., Getzewich, B., Guignard, A., Heidinger, A., Maddux, B. C., Menzel, W. P., Minnis, P., Pearl, C., Platnick, S., Poulsen, C., Riedi, J., Sun-Mack, S., Walther, A., Winker, D., Zeng, S., and Zhao, G.: Assessment of Global Cloud Datasets from Satellites: Project and Database Initiated by the GEWEX Radiation Panel, BAMS, 94, 1031–1049, https://doi.org/10.1175/BAMS-D-12-00117.1, 2013.

Tarrio, K., Tang, X., Masek, J. G., Claverie, M., Ju, J., Qiu, S., Zhu, Z., and Woodcock, C. E.: Comparison of cloud detection algorithms for Sentinel-2 imagery, Science of Remote Sens., 2, 100 010, https://doi.org/https://doi.org/10.1016/j.srs.2020.100010, 2020.

https://doi.org/10.5194/egusphere-2023-1834
Preprint. Discussion started: 16 August 2023

Thies, B. and Bendix, J.: Satellite based remote sensing of weather and climate: recent achievements and future perspectives, Meteorol. Appl., 18, 262–295, https://doi.org/10.1002/met.288, 2011.

van den Heuvel, F., Foresti, L., Gabella, M., Germann, U., and Berne, A.: Learning about the vertical structure of radar reflectivity using hydrometeor classes and neural networks in the Swiss Alps, Atmos. Meas. Tech., 13, 2481–2500, https://doi.org/10.5194/amt-13-2481-2020, 2020.

Vial, J., Dufresne, J.-L., and Bony, S.: On the interpretation of inter-model spread in CMIP5 climate sensitivity estimates, Clim. Dyn., 41, 3339–3362, https://doi.org/10.1007/s00382-013-1725-9, 2013.

Wang, F., Liu, Y., Zhou, Y., Sun, R., Duan, J., Li, Y., Ding, Q., and Wang, H.: Retrieving Vertical Cloud Radar Reflectivity from MODIS Cloud Products with CGAN: An Evaluation for Different Cloud Types and Latitudes, Remote Sens., 15, 816, https://doi.org/10.3390/rs15030816, 2023.

Wang, G., Wang, H., Zhuang, Y., Wu, Q., Chen, S., and Kang, H.: Tropical Overshooting Cloud-Top Height Retrieval from Himawari-8 Imagery Based on Random Forest Model, Atmosphere, 12, https://doi.org/10.3390/atmos12020173, 2021.

Wang, S., Chen, W., Xie, S. M., Azzari, G., and Lobell, D. B.: Weakly Supervised Deep Learning for Segmentation of Remote Sensing Imagery, Remote Sens., 12, https://doi.org/10.3390/rs12020207, 2020.

Wang, Z., Zhao, J., Zhang, R., Li, Z., Lin, Q., and Wang, X.: UATNet: U-Shape Attention-Based Transformer Net for Meteorological Satellite Cloud Recognition, Remote Sens., 14, https://doi.org/10.3390/rs14010104, 2022.

Watson-Parris, D.: Machine learning for weather and climate are worlds apart, Philos. Trans. Royal Soc. A, 379, 20200098, https://doi.org/10.1098/rsta.2020.0098, 2021.

Wieland, M., Li, Y., and Martinis, S.: Multi-sensor cloud and cloud shadow segmentation with a convolutional neural network, Remote Sens. Environ., 230, https://doi.org/10.1016/j.rse.2019.05.022, 2019.

Zhang, D., He, Y., Li, X., Zhang, L., and Xu, N.: PrecipGradeNet: A New Paradigm and Model for Precipitation Retrieval with Grading of Precipitation Intensity, Remote Sens., 15, https://doi.org/10.3390/rs15010227, 2023.

Zhang, Z., Ackerman, A. S., Feingold, G., Platnick, S., Pincus, R., and Xue, H.: Effects of cloud horizontal inhomogeneity and drizzle on remote sensing of cloud droplet effective radius: Case studies based on large-eddy simulations, J. Geophys. Res. Atmos., 117, https://doi.org/https://doi.org/10.1029/2012JD017655, 2012.